

Supporting information

Low molecular-weight carbon nitrides for solar hydrogen evolution

Vincent Wing-hei Lau†§, Maria B. Mesch‡, Viola Duppel†§, Volker Blum||, Jürgen Senker‡, Bettina V. Lotsch†§⊥*

† Max Planck Institute for Solid State Research, Heisenbergstraße 1, 70569 Stuttgart, Germany

‡ Department of Inorganic Chemistry III, University of Bayreuth, Universitätsstraße 30, 95447 Bayreuth, Germany

§ Department of Chemistry, University of Munich, Butenandtstraße 5-13, 81377 Munich, Germany

|| Department of Mechanical Engineering and Materials Science and Center for Materials Genomics, Duke University, Durham, North Carolina 27708, United States

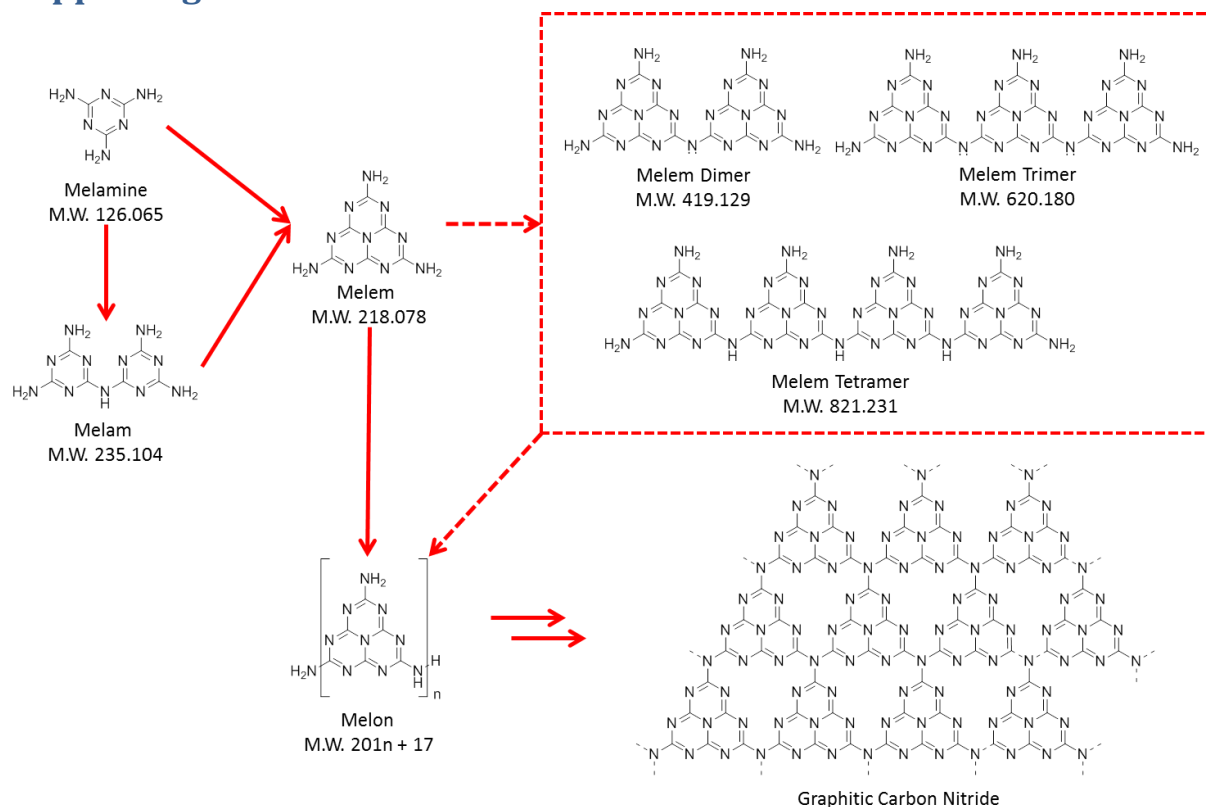
⊥ Nanosystems Initiative Munich (NIM) and Center for Nanoscience, Schellingstraße 4, 80799 Munich, Germany

Table of content

Contents

Supporting introduction	2
Experimental section.....	3
Computational details & additional discussions	6
Characterization of as-synthesized melem oligomer	7
Characterization of as-synthesized melem oligomer after the photocatalytic reaction.....	9
Characterization of the fractions separated from the as-synthesized melem oligomer.....	12

Supporting introduction



Scheme S1 Route of condensation from melamine to melem, directly or via melam, then to the linear polymer melon. The idealized structure of graphitic carbon nitride is also shown as a hypothesised product of complete melem condensation, as indicated by the double arrow. Scheme adapted from Schwarzer *et al.*¹

Experimental section

Syntheses were carried out by loading the precursor in an alumina boat (volume 1.8 cm³) covered with alumina crucibles (not airtight) to prevent excess sublimation of the precursor (headspace ≈3 cm³). The alumina boat was placed in the centre of a quartz tube (diameter 28 mm, length 650 mm) inside a tube furnace operated by a temperature controller (Eurotherm 2408) using resistive heating. Air was removed by extended flushing of the quartz tube with argon. Argon flow was reduced to about 0.5 cm³ s⁻¹ prior to the heating program.

X-ray diffraction patterns were collected using a STOE Stadi P diffractometer (Cu K α 1) in transmission mode. ATR-IR spectra were collected with a PerkinElmer UATR TWO spectrometer equipped with a diamond crystal. Diffuse reflectance UV-Vis spectra were collected on a Cary 5000 spectrometer (referenced to PTFE or barium sulfate) and the spectra in percentage reflectance were converted using the Kubelka Munk function. CHN elemental analyses were performed with a Vario El element analyzer (Elementar Analysensysteme GmbH). Oxygen content analyses were performed using a carrier gas heat extraction analyzer (TC-436, LECO) as follows. The sample in a metallic flux (nickel and tin) was heated in a graphite crucible to 2500 °C under helium flow and the oxygen was quantified by IR absorption as CO₂. Surface areas were calculated using Brunauer–Emmett–Teller (BET) theory from the argon adsorption isotherms of the samples. Samples were outgassed for 6–12 h overnight at 100 °C to a vacuum of 10⁻⁷ mbar. Isotherms were collected on a Quantachrome Autosorb iQ gas sorption analyzer using argon as the sorbent at 87.45 K.

Solid-state magic angle spinning NMR was performed at ambient temperature on an AvanceIII HD 600 and an AvanceIII HD 400 solid state NMR spectrometer (Bruker) with an external magnetic field of 14.1 T and 9.4 T, respectively. The operating frequencies of the two spectrometers are 600.1 MHz, 150.9 MHz, 60.8 MHz and 400.1 MHz, 100.6 MHz, 40.6 MHz for ¹H, ¹³C and ¹⁵N, respectively. The samples were contained either in 1.9 mm or 4 mm ZrO₂ rotors, which were mounted in standard triple or double resonance MAS probes (Bruker). The spinning speed was set to 15 kHz for the 1.9 mm rotor, or 5 kHz for the 4 mm rotor. ¹³C and ¹⁵N spectra were recorded using standard or ramped amplitude cross polarization (CP) with contact times of 10 and 15 ms, respectively. The recycle delay was set to 4s for ¹³C and to 3s for ¹⁵N measurements. All spectra were referenced to TMS for the ¹³C and nitromethane for ¹⁵N. During acquisition of ¹³C and ¹⁵N proton decoupling was carried out using SPINAL64 with an rf field between 70 and 80 kHz.

MALDI-TOF (matrix-assisted laser desorption/ionization-time of flight) was performed on a Shimadzu Axima Resonance mass spectrometer. Calibration was carried out using neat fullerene and using CsI ground with trans-2-[3-(4-*tert*-butylphenyl)-2-methyl-2-propenylidene]malononitrile as the matrix. Each sample was ground with tetracyanoquinodimethane (TCNQ) as the matrix and deposited on a steel sample holder. The spectra were collected in raster mode and the laser power was progressively increased until a suitable signal-to-noise ratio was achieved. The spectra presented are averaged from 100 profiles.

Transmission electron microscopy (TEM) was performed with a Philips CM30 ST (300 kV, LaB6 cathode). The samples were suspended in n-butanol and drop-cast onto a lacey carbon film (Plano). Scanning electron microscopy (SEM) was performed on a Vega TS 5130MM (Tescan) microscope equipped with an energy dispersive detector for X-ray spectroscopy (EDX, Oxford Instrument). Each

sample was deposited onto a carbon tab (Leco) and sputtered with gold for imaging. No sputtering was used for elemental analysis by EDX.

Zeta potential was measured using a Malvern Zetasizer Nano ZS. The sample was dispersed with sonication in NaCl solution (10 mM) of different pH (adjusted with HCl or NaOH) and allowed to stand prior to measurements in disposable cuvettes (Malvern). Measurements were conducted as four replicates; average results were quoted using the standard deviation as the error.

For X-ray photoelectron spectroscopy (XPS), samples were pressed onto indium foil and the spectra were collected on an Axis Ultra (Kratos Analytical, Manchester) X-ray photoelectron spectrometer with charge neutralization. The spectra were processed using the software OriginPro 8.5.1. All peaks were fitted using a Gaussian function with baseline correction, except for platinum, where a Gaussian-Lorentzian function was used. The spectra were referenced with the adventitious carbon 1s peak at 284.80 eV. Binding energies were compared with the NIST Standard Reference Database 30 (Version 4.1) unless otherwise specified.

Thermogravimetric analysis coupled with mass spectroscopy (TGA-MS) was performed with the instrument STA 409 C (Netzsch GmbH, Selb, Germany) connected with a quadrupole mass spectrometer QMS 422 (Balzers, Hudson, USA). Samples were loaded in alumina crucibles and heated under argon (100 mL min^{-1}) from ambient temperature to $900 \text{ }^\circ\text{C}$ at a ramp rate of $1 \text{ }^\circ\text{C min}^{-1}$. To separate the contributions of ammonia and hydroxide (from background moisture) of the $m/z = 17$ signal, a blank, reference measurement was carried out to determine the ratio of the water to hydroxide signal. The ammonia contribution to the $m/z = 17$ signal was then calculated by subtracting the $m/z = 18$ signal multiplied by the water-hydroxide ratio.

Photoluminescence (PL) spectra were collected in excitation mode with a Horiba FluoroLog F3-22 spectrophotometer at 90° to the excitation source. The powder samples ($1.0 \pm 0.1 \text{ mg}$) were suspended with sonication in an aqueous methanol solution (10 vol%, 3 mL) and the suspension was measured in a quartz cuvette. Excitation wavelengths employed were 260 nm for the melon sample and 250 nm for the oligomeric samples. These wavelengths were identified to maximize the PL signal using emission mode.

Photocatalytic experiments were performed in a double-walled glass reactor (Figure S1), where the outer compartment is circulated with thermostated water ($25 \text{ }^\circ\text{C}$). The reactor was top-irradiated through a quartz window with a xenon lamp (Newport, 300 W) equipped with a water filter and either a dichroic mirror that allows only visible light ($\lambda > 420 \text{ nm}$) to pass or a full spectrum mirror ($2000 \text{ nm} > \lambda > 200 \text{ nm}$). An air mass (AM) 1.5 filter was also used where specified. For each experiment, the catalyst powder (20 mg) was suspended in a phosphate buffer solution (PBS, 18 mL of 0.1 M solution at pH 3, 7 or 11) containing methanol (2 mL). Dihydrogen hexachloroplatinate ($5 \text{ } \mu\text{L}$, 8 wt% aqueous solution, Aldrich) was added for the *in-situ* formation of platinum as the cocatalyst, which yields a loading of around 2 wt%. The headspace was subjected to several cycles of evacuation and argon backfill prior to the experiment. In the course of the experiment, the headspace of the reactor was periodically sampled and the components were quantified by gas chromatography (Thermo Scientific TRACE GC Ultra) equipped with a TCD detector using argon as the carrier gas. After the photocatalytic experiment, the catalyst was recovered by centrifugation, washed with water, then dried at $100 \text{ }^\circ\text{C}$. Experiments for the estimation of quantum efficiencies were conducted using band pass filters with band centers at 400 nm and 500 nm with full width half

maximum of 50 nm (Thorlab). Irradiance of the incident light was measured using a thermopile (Thorlabs). The apparent quantum efficiency was then calculated as:

$$AQE [\%] = \frac{2 \times \text{Hydrogen evolution rate} [\text{mol } h^{-1}]}{\text{Photon flux} [\text{mol } h^{-1}]}$$

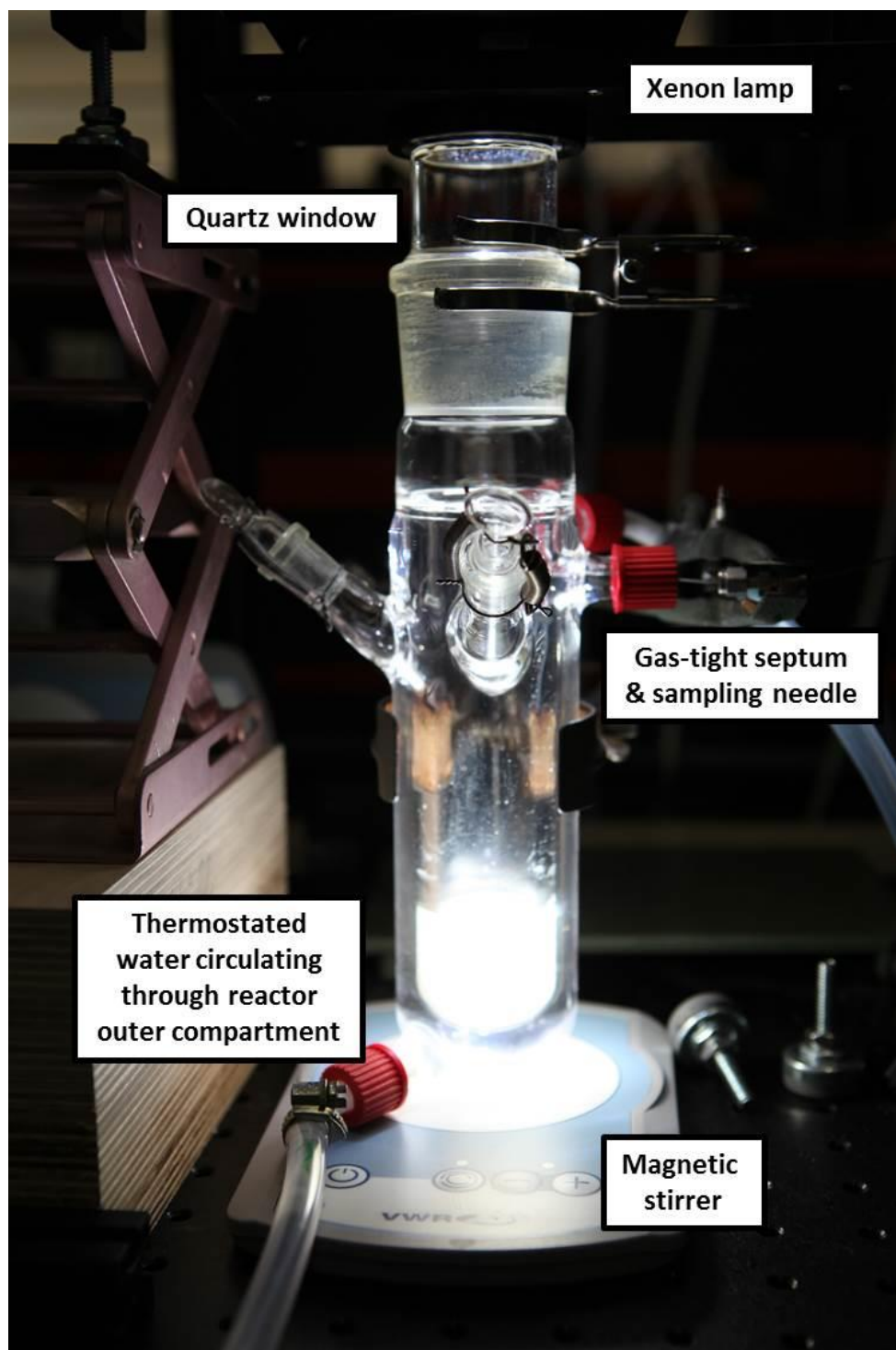


Figure S1 Reactor set-up used for evaluating photocatalysts for hydrogen evolution.

Computational details & additional discussions

Calculations were performed with the FHI-aims all-electron electronic structure code.^{2,3} For the heptazine monomer, dimer, trimer, and tetramer, minimum-energy geometries were calculated using the van der Waals corrected DFT-generalized gradient approximation (GGA) with the PBE functional^{4,5} and "tight" numerical settings ("tier 2" basis sets in FHI-aims). The isolated tetramer allows for significant conformation flexibility, as exemplified by four specific prototypes in Table S4.

For the calculation of HOMO and LUMO levels of the isolated conformers (vacuum), a recently developed, approximate approach⁶ to parameterize the PBE hybrid (PBEh) density functional⁷ for molecular systems was employed. In brief, so-called G^0W^0 -level many-body perturbation theory (MBPT) calculations³ were carried out for effective single quasi-particle levels of the monomer, based on the electronic structure derived from PBEh functional with different exact exchange mixing parameters $0 \leq \alpha \leq 1$ and using highly converged NAO-VCC-5Z basis sets,⁸ developed specifically for reliable convergence of the unoccupied-state sums necessary for MBPT. Following reference 6, a value $\alpha=0.6882$ was determined, for which the monomer HOMO level as evaluated by the PBEh functional and by the G^0W^0 calculation agree. This optimized PBEh functional ($\alpha=0.6882$) was then used to calculate HOMO and LUMO orbitals and energy levels for the isolated (vacuum) conformers of the dimer, trimer, and tetramer, using FHI-aims "tight" settings and a tier 2 basis set.

The effective single-quasiparticle levels of isolated gas phase molecules cannot be directly compared to UV-Vis absorption spectra or PL spectra obtained in the condensed phase, but the relative development of the HOMO/LUMO levels with conformer length and conformation can be compared as a trend. Table S3 lists HOMO, LUMO, and band gap values as calculated for the isolated conformers shown in Figure 6 in the main paper (optimized PBEh values; PBE values in brackets). Table S4 shows examples of types of tetramer conformers and their HOMO, LUMO, and gap values. The orbital isosurfaces shown were calculated using the optimized PBEh functional. As these calculations were carried out for an isolated molecule in vacuum, they serve to illustrate how conformation and inter/intramolecular variations can lead to changes in HOMO/LUMO distribution and energy gap. More detailed calculations require other factors (solvent effect, electron-phonon coupling, excitonic effects) to be taken into account to fully reflect the material under photocatalytic conditions.

The two different treatments yield very different absolute values for the gas phase frontier orbital energy levels, with the optimized PBEh values likely closer to the truth for the isolated molecules. In contrast, the experimentally measured UV-Vis gaps contain a variety of other effects due to the condensed phase, including the effect of the surrounding medium (solvent shift), renormalization by electron-phonon coupling or excitonic effects, etc. The trend of the HOMO, LUMO, and gap values with conformer length (smaller gap with increasing length) is consistent between both density functional descriptions used and also with the experiments. We stress that the overall shape (geometry) of the HOMO, LUMO, and molecular conformation are much less affected by the choice of functional than the actual eigenvalues.

Characterization of as-synthesized melem oligomer

Values for the quantum efficiencies were estimated using the incident photon across the entire AM 1.5 spectrum up to where the water filter cuts off the infrared portion. The melem oligomer and the melon have a quantum efficiency of approximately 0.015% and 0.0051%, respectively. The apparent deactivation of the photocatalysts in alkaline solution is attributed to the formation of CO in the oxidation of methanol in a basic environment, which can irreversibly bind to the platinum co-catalyst.⁹

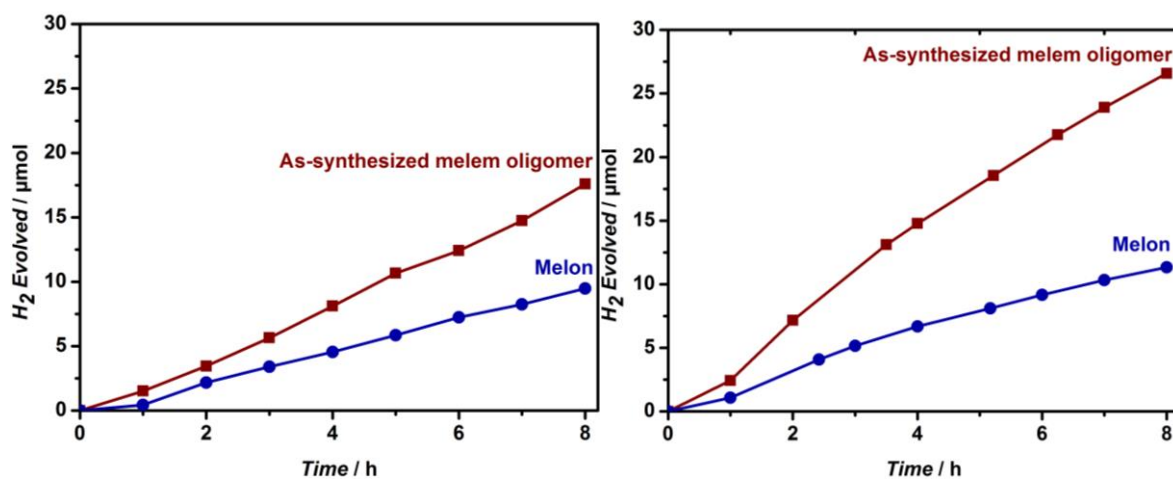


Figure S2 Photocatalytic hydrogen evolution of the melem oligomer, compared with melon, in PBS of pH 3 (left) and pH 11 (right). The full spectrum of the xenon lamp, together with the AM 1.5 filter, was used.

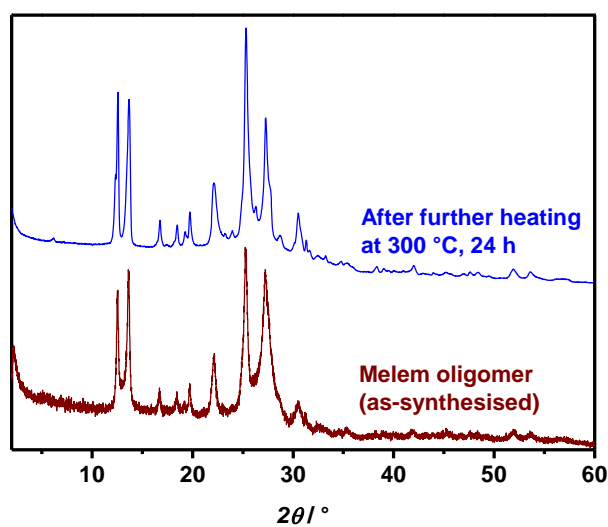


Figure S3 XRD pattern of melem oligomer after further heat treatment.

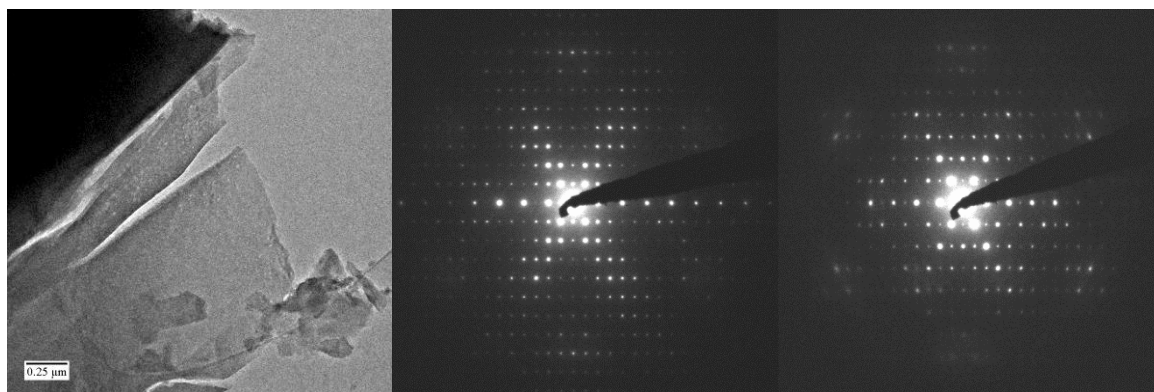


Figure S4 TEM image (left) and precession electron diffraction patterns (center and right) of the as-synthesized melem oligomer sample after heat treatment for improved crystallinity. The pattern in the center can be assigned to melem, viewed along the [100] zone axis. The pattern on the right is an unknown phase and has a unit cell slightly elongated in the [001] direction and contracted in the [010] direction compared to melem.

Table S1 Elemental analyses of the melem oligomer and melon in comparison with theoretical values for melem and ideal C_3N_4 . The reported values and their uncertainties are the average and standard deviation, respectively, of three replicates.

	C (wt%)	N (wt%)	H (wt%)	O (wt%)	C:N atomic ratio
Melem (th.)	33.0	64.2	2.8	0	0.60
As-synthesized melem oligomer	33.78±0.05	58.9±0.5	2.5±0.1	1.75±0.04	0.67
Melon	35.40±0.08	60.6±0.5	1.83±0.05	0.8±0.1	0.68
Melon (th. 1D polymer)	35.8	62.7	1.5	0	0.66
C_3N_4 (th.)	39.1	60.9	0	0	0.75

Characterization of as-synthesized melem oligomer after the photocatalytic reaction

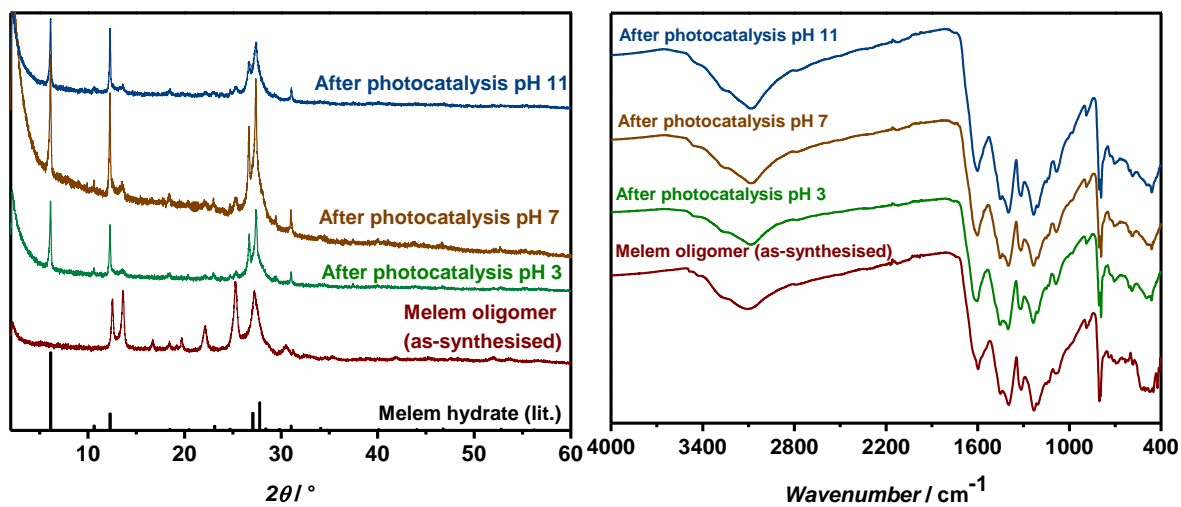


Figure S5 XRD patterns (left) and ATR-IR spectra (right) of melem oligomer before and after photocatalysis.

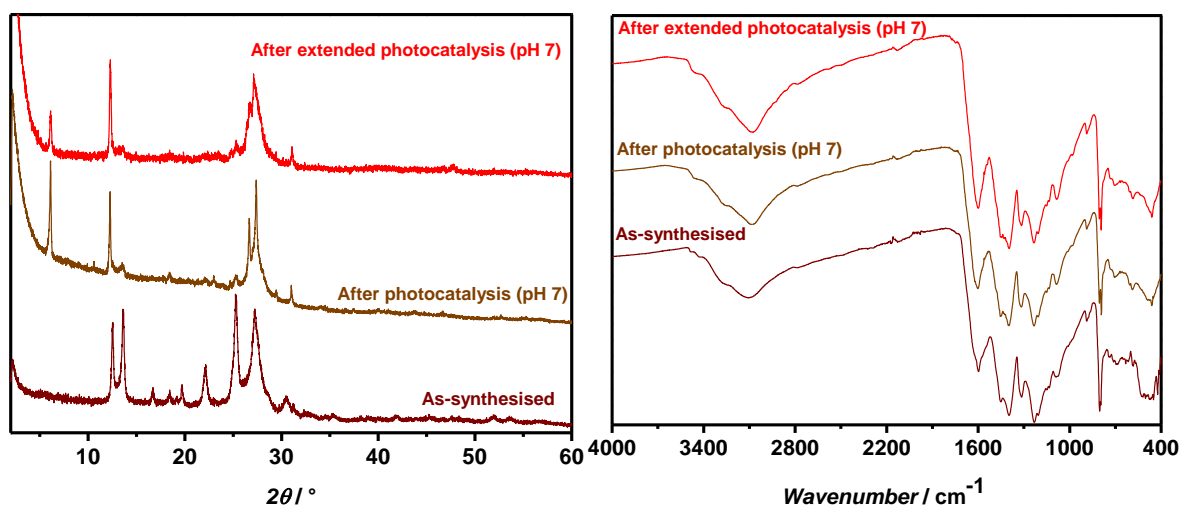


Figure S6 Characterization of the melem oligomer after the 129 h extended photocatalytic test (Figure 1b) by XRD (left) and ATR-IR (right).

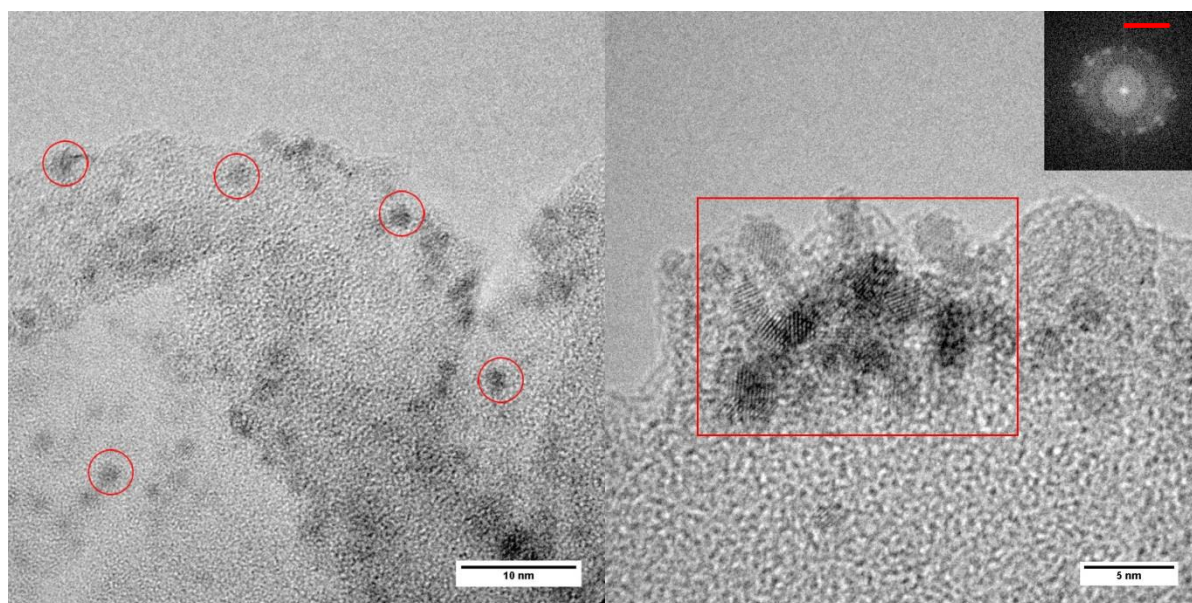


Figure S7 HRTEM images of the as-synthesized melem oligomer after the extended (>120 h) photocatalytic reaction. The left image shows an overview with some platinum particles marked; these spherical particles are generally less than 2 nm in diameter. The right image is a magnified view showing a cluster of platinum particles; the fast fourier transform of the region inside the red box is shown in the inset, where the red line shows the radius of the ring is $\approx 2.3 \text{ \AA}$, corresponding to the (111) d -spacing of platinum.

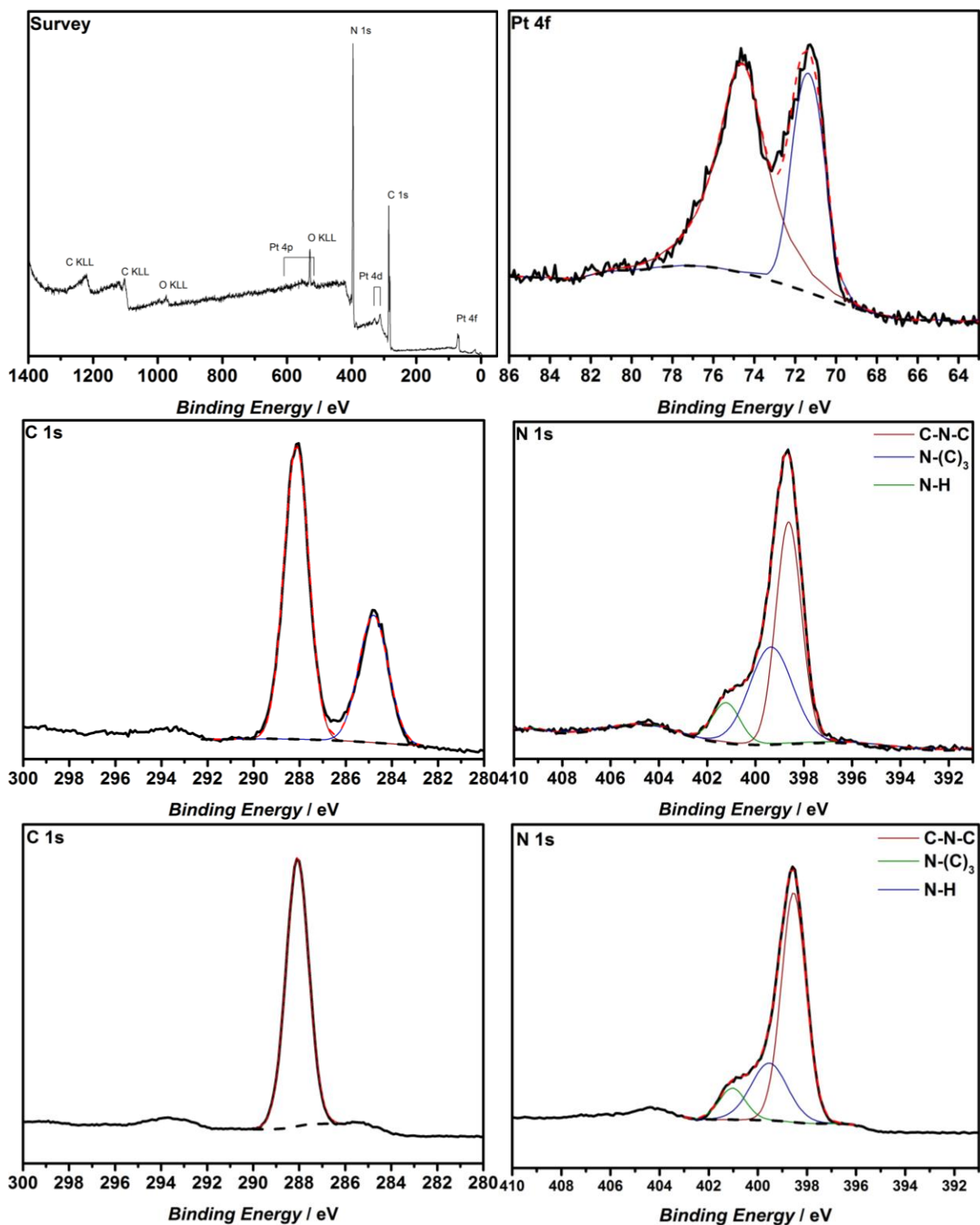


Figure S8 XPS spectra of the as-synthesized melem oligomer after extended (>120 h) photocatalytic reaction: survey spectrum (top left); Pt 4f region (top right); C 1s and N 1s regions (middle left and right respectively). For comparison, the C 1s and N 1s regions of the sample before the catalytic reactions are shown in the bottom left and right, respectively. Note that the C 1s peak at the lower binding energy is assigned to the adventitious carbon and is calibrated to 288.4 eV.

Characterization of the fractions separated from the as-synthesized melem oligomer

Table S2 BET surface areas, hydrogen evolution rates and apparent quantum efficiencies of the fractions, compared with the as-synthesized sample and melon.

	BET surface area (m ² g ⁻¹)	H ₂ evolution rate (μmol h ⁻¹)	Apparent quantum efficiency at 400 (±25) nm (%)
Melem oligomer (as-synthesised)	14.0 ± 0.5	2.8	*
DMSO soluble fraction	14.7 ± 0.5	0.0	*
RCF 10000 fraction	23.3 ± 0.3	4.8	8.7×10 ⁻²
RCF 60000 fraction	24.6 ± 1.4	5.4	1.0×10 ⁻¹
Melon	9.0 ± 0.2	0.6	1.5×10 ⁻²

*Not measured

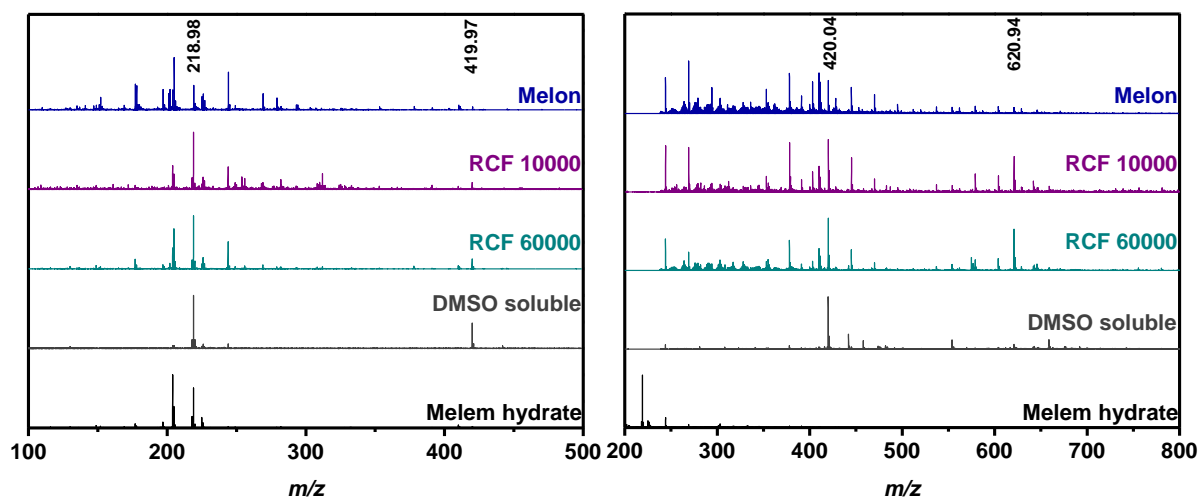


Figure S9 MALDI-TOF spectra of the fractions, compared with melem and melon, measured in the mass range >100 (left) and >300 (right). The signal at 203.94 corresponds to the matrix.

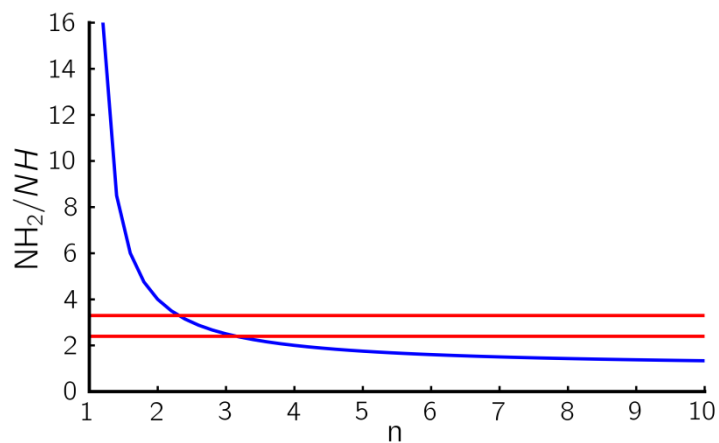


Figure S10 Plot of the integral ratio $^{15}\text{NH}_2 : ^{15}\text{NH}$ against the chain length n . Red lines indicate the experimental values. The ratio was calculated according to the formula $\frac{\text{NH}_2}{\text{NH}} = \frac{n+2}{n-1}$.

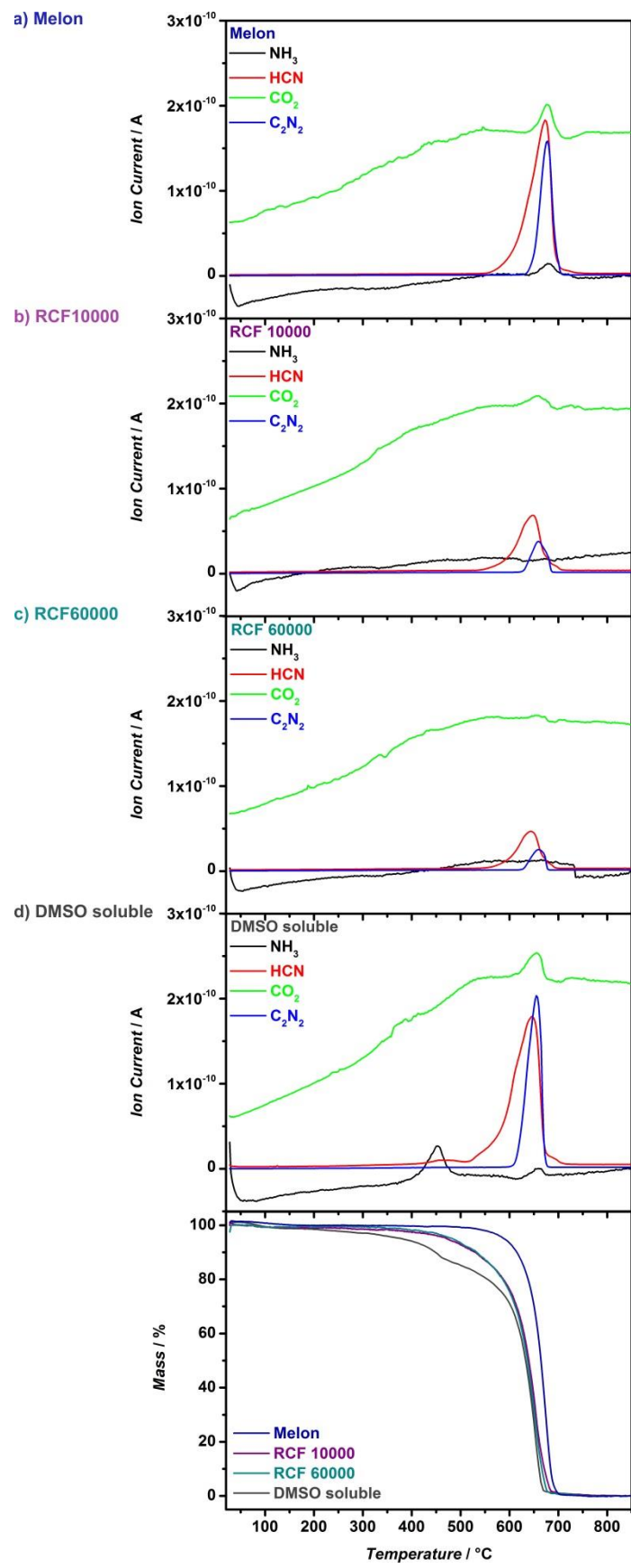


Figure S11 TGA-MS analyses of: a) melon; b) RCF 10000 fraction; c) 60000 fraction; and d) the DMSO soluble fraction. Samples were heated at $1 \text{ }^\circ\text{C min}^{-1}$ under argon.

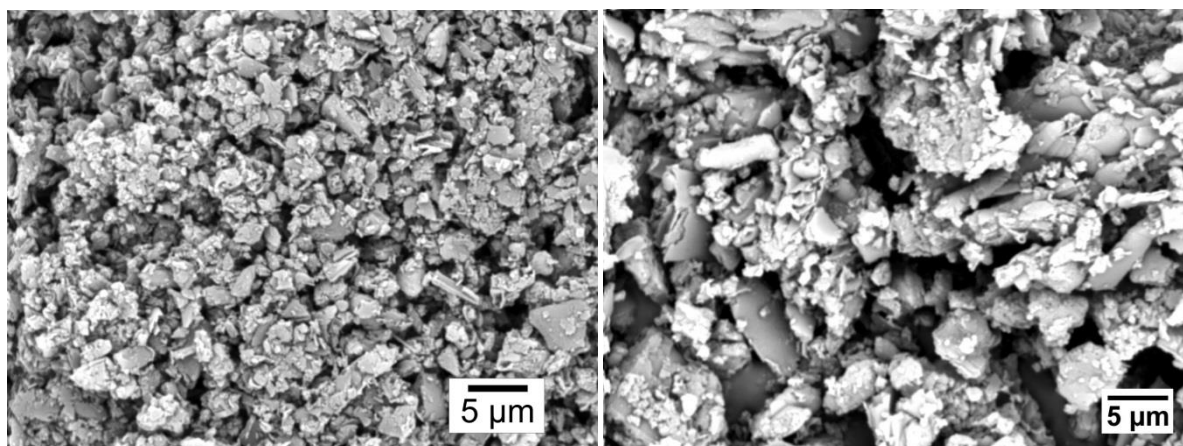


Figure S12 SEM image of the fraction obtained at RCF 60000 (left) and melon (right).

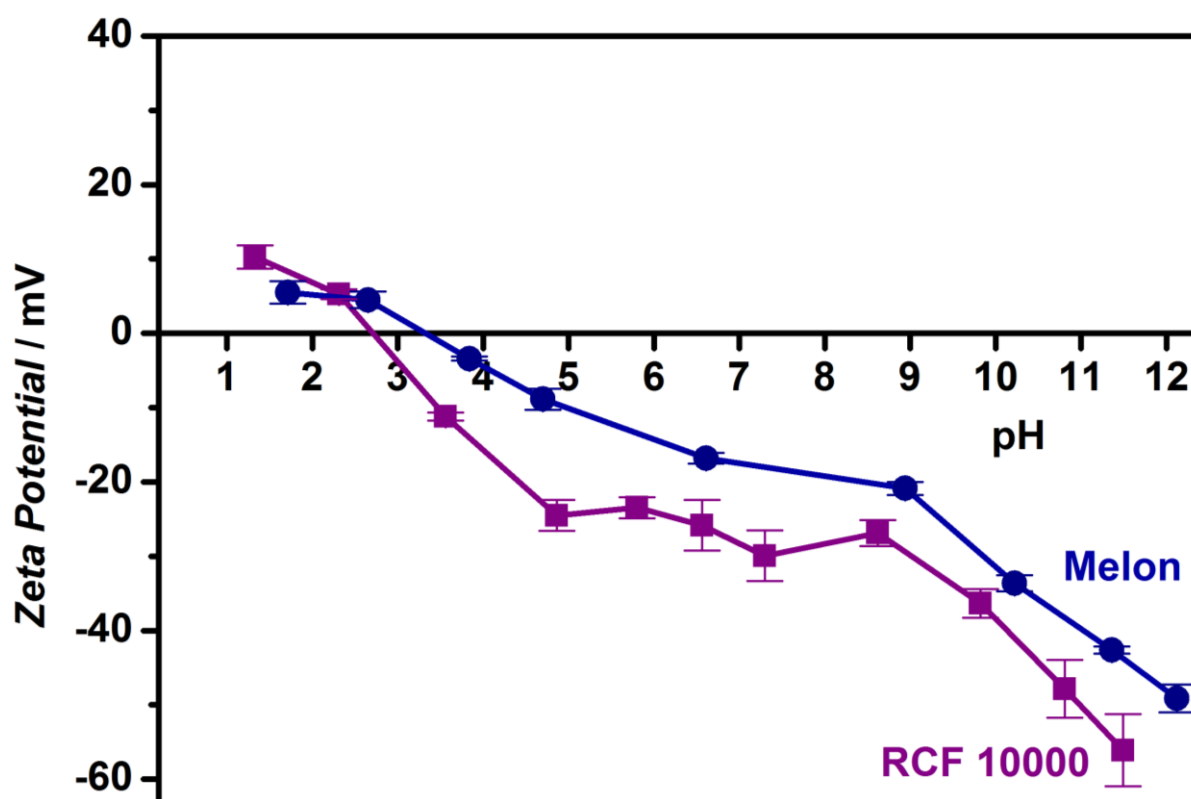


Figure S13 Plot of zeta potential versus pH for the fraction RCF 10000 compared to the polymer melon. Isoelectric points for this fraction and melon are at pH 2.7 and 3.3, respectively.

Table S3 Orbital energies for the calculated structures in Figure 7. Potential energies are referenced to vacuum. Optimized PBEh functional eigenvalues (PBE values in brackets).

	HOMO (eV)	LUMO (eV)	Energy Gap (eV)
Monomer	-8.695 (-5.602)	+0.285 (-2.105)	8.980 (3.497)
Dimer	-8.783 (-5.711)	-0.638 (-2.776)	8.145 (2.935)
Trimer	-8.825 (-5.760)	-0.894 (-2.984)	7.931 (2.776)
Tetramer	-8.847 (-5.780)	-1.014 (-3.085)	7.833 (2.695)

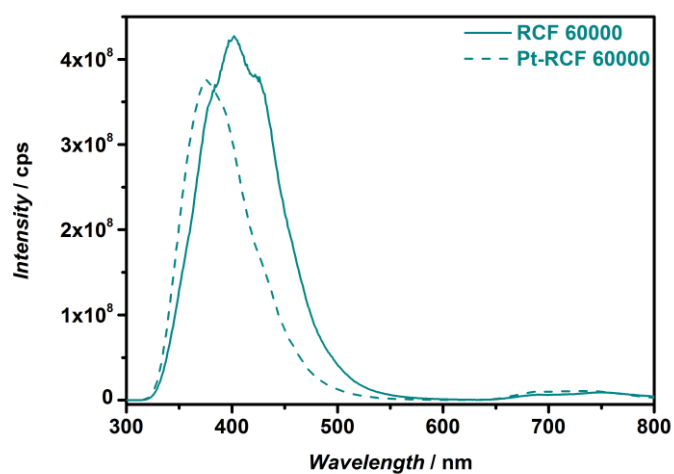
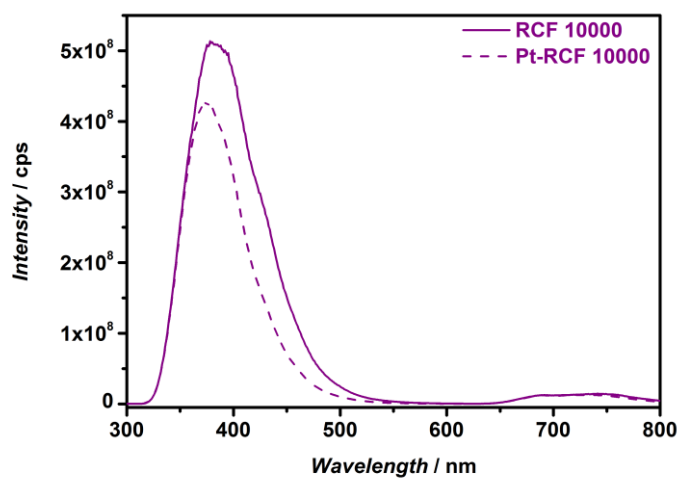
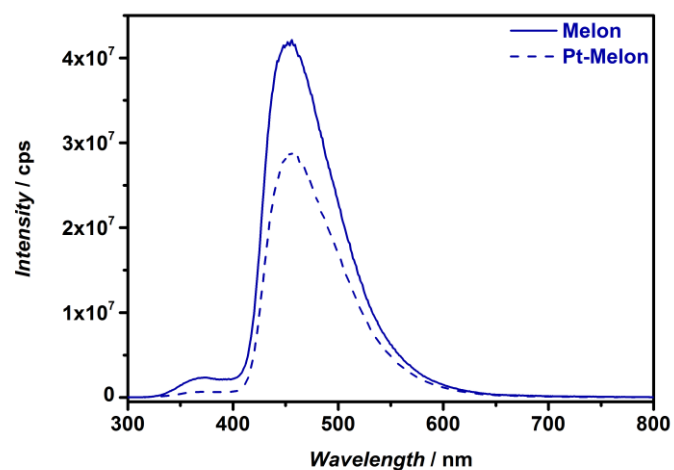
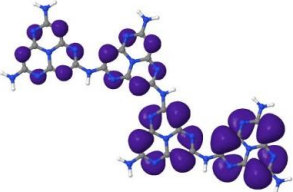
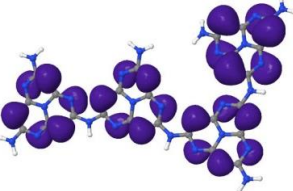
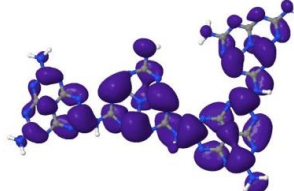
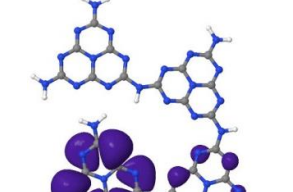
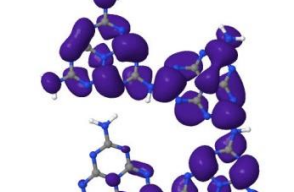
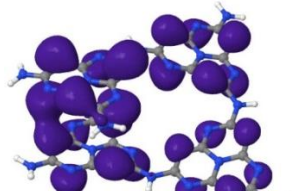
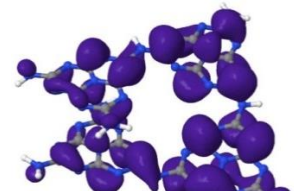


Figure S14 Photoluminescence spectra of melon and the oligomeric fractions suspended in aqueous methanol (10 vol%) with and without platinum loading.

Table S4 Variations of energy levels (versus vacuum) and gaps depending on tetramer conformation and hydrogen bonding. The potential values provided are derived from the optimized PBEh hybrid density functional with $\alpha = 0.6882$, while the values in brackets are derived using the PBE functional. Only the positive parts of the HOMO and LUMO orbitals are shown. The negative parts are located on the respective opposite sides of the heptazine planes and are omitted in order to show the locations of individual atoms more clearly.

Conformer	HOMO	LUMO	HOMO (eV)	LUMO (eV)	Energy Gap (eV)
Planar staggered			-8.834 (-5.762)	-1.012 (-3.084)	7.822 (2.678)
Twisted			-8.851 (-5.780)	-1.013 (-3.091)	7.838 (2.689)
Hydrogen bonded			-8.635 (-5.548)	-1.040 (-3.139)	7.595 (2.409)
Helical π -stacked			-8.841 (-5.708)	-0.987 (-3.084)	7.854 (2.624)

- (1) Schwarzer, A.; Saplinova, T.; Kroke, E. *Coord. Chem. Rev.* **2013**, *257*, 2032
- (2) Blum, V.; Gehrke, R.; Hanke, F.; Havu, P.; Havu, V.; Ren, X.; Reuter, K.; Scheffler, M. *Comput. Phys. Commun.* **2009**, *180*, 2175
- (3) Ren, X.; Rinke, P.; Blum, V.; Wieferink, J.; Tkatchenko, A.; Sanfilippo, A.; Reuter, K.; Scheffler, M. *New J. Phys.* **2012**, *14*, 053020
- (4) Perdew, J. P.; Burke, K.; Ernzerhof, M. *Phys. Rev. Lett.* **1996**, *77*, 3865
- (5) Tkatchenko, A.; Scheffler, M. *Phys. Rev. Lett.* **2009**, *102*, 073005
- (6) Atalla, V.; Yoon, M.; Caruso, F.; Rinke, P.; Scheffler, M. *Phys. Rev. B* **2013**, *88*, 165122
- (7) Perdew, J. P.; Ernzerhof, M.; Burke, K. *Journal of Chemical Physics* **1996**, *105*, 9982
- (8) Zhang, I. Y.; Ren, X.; Rinke, P.; Blum, V.; Scheffler, M. *New J. Phys.* **2013**, *15*, 123033
- (9) Spendelow, J. S.; Goodpaster, J. D.; Kenis, P. J. A.; Wieckowski, A. *Langmuir* **2006**, *22*, 10457